JOURNAL OF THERMOPHYSICS AND HEAT TRANSFER
Vol. 23, No. 2, April–June 2009

Optical Emission Spectroscopy During Plasmatron Testing of ZrB_2–SiC Ultrahigh-Temperature Ceramic Composites

Mickaël Playez* and Douglas G. Fletcher†
von Kármán Institute for Fluid Dynamics, 1640 Rhode-Saint-Genèse, Belgium
Jochen Marschall‡
SRI International, Menlo Park, California 94025
and
William G. Fahrenholtz,§ Greg E. Hilmas,¶ and Sumin Zhu**
Missouri University of Science and Technology, Rolla, Missouri 65409

DOI: 10.2514/1.39974

Optical emission spectroscopy is used to investigate the oxidation of a hot-pressed ZrB_2–SiC ultrahigh-temperature ceramic composite tested in the 1.2 MW Plasmatron facility at the von Kármán Institute for Fluid Dynamics. Time-resolved spectra enable the in situ detection and temporal characterization of electronically excited B, BO, and BO_2 species concentrations directly adjacent to the oxidizing sample surface. The evolution of these boron species correlates well with the transient formation of a complex multilayer oxide scale containing a silica-rich glassy outer layer that limits oxide growth.

Nomenclature

a	=	activity
$\dot{m}$	=	mass flow rate, $kg \cdot s^{-1}$
P	=	pressure, Pa
q	=	heat flux, $W \cdot m^{-2}$
R	=	universal gas constant, $8.314\ J \cdot mol^{-1} \cdot K^{-1}$
T	=	temperature, K

Subscripts

cw	=	cold wall
dyn	=	dynamic
stat	=	static
w	=	wall

I. Introduction

ULTRAHIGH-TEMPERATURE ceramic (UHTC) composites based on the diborides ZrB_2 and HfB_2 in combination with silica-forming refractory materials like SiC and $MoSi_2$ are under active study for high-temperature aerospace applications on hypersonic vehicles [1,2]. Both ZrB_2 and HfB_2 have extremely high melting points (3245 and 3380°C, respectively) [3] and relatively high thermal conductivities ($80 \pm 40\ W \cdot m^{-1} \cdot K^{-1}$) [4,5], making them potentially enabling for shape-stable leading-edge and control surface components for which extreme aerothermal heating rates lead to the failure of conventional aerospace materials.

In high-temperature oxidizing environments, ZrB_2 and HfB_2 react with oxygen to form transition metal and boron oxides according to the reaction

$$(Zr, Hf)B_2 + 5/2O_2 \rightarrow (Zr, Hf)O_2 + B_2O_3 \qquad (1)$$

Both ZrO_2 and HfO_2 are refractory materials with melting points above 2500°C. However, crystalline B_2O_3 melts at 450°C, and the softening temperature for amorphous B_2O_3 glass is reported to lie between 560 and 630°C [6]. The vapor pressure of liquid B_2O_3 rises rapidly as temperature increases, reaching an atmospheric pressure boiling point at about 2080°C [7].

Furnace studies of ZrB_2 in air generally reveal parabolic oxidation rates at temperatures below ~1100°C, indicating that liquid B_2O_3 permeates the porous transition metal oxide layer and seals the surface, limiting inward oxygen transport [8–11]. With increasing temperature, volatilization of the protective B_2O_3 liquid leads to more rapid oxidation. At temperatures above ~1400°C, the loss of B_2O_3 by evaporation is so rapid that the porous transition metal oxide layer may be exposed. When this occurs, the oxide scale no longer limits oxygen transport effectively and the ZrB_2 oxidation rates can become linear. The addition of a silica former improves the oxidation resistance of ZrB_2 (and HfB_2) at temperatures above 1100°C with the formation of amorphous SiO_2, which has a much lower volatility than B_2O_3 and performs the same sealing function [11–15]. At 1500°C, B_2O_3 has a vapor pressure of about 233 Pa, compared with 3×10^{-4} Pa for silica [16].

The most-studied diboride-based UHTC composites contain between 10 and 30 vol % SiC. When oxidized, these materials form a multilayer oxide scale with an outer silica-rich glassy layer and an inner SiC-depleted layer, separated at times by a thin layer of ZrO_2 entrained in SiO_2 [11,17–20]. The relative thicknesses of the different layers depend on test conditions such as time, temperature, gas composition, etc. The formation of this complex oxide structure has been rationalized using thermodynamic calculations and species transport arguments [16,21,22] supported by posttest sample

Received 23 July 2008; revision received 7 January 2009; accepted for publication 18 January 2009.

*Senior Research Engineer, Aeronautics and Aerospace Department, Chaussee de Waterloo 72; playez@vki.ac.be Member AIAA.
†Past Head, Aeronautics and Aerospace Department; currently, Professor, Mechanical Engineering, University of Vermont, 201 Votey Hall, 33 Colchester Avenue, Burlington, VT, 05405; douglas.fletcher@uvm.edu. Associate Fellow AIAA.
‡Senior Research Scientist, Molecular Physics Laboratory, 333 Ravenswood Avenue; jochen.marschall@sri.com. Senior Member AIAA.
§Professor, Department of Materials Science and Engineering, 223 McNutt Hall; billf@mst.edu.
¶Professor, Department of Materials Science and Engineering, 223 McNutt Hall; ghilmas@mst.edu.
**Ph.D. Candidate, Department of Materials Science and Engineering, 223 McNutt Hall; Sumin.Zhu@us.vesuvius.com.

characterization that typically uses regular or field-emission scanning electron microscopy (FESEM), energy dispersive x-ray spectroscopy (EDS), and x-ray diffraction.

The oxidation of hot-pressed ZrB_2 composites containing 30 vol % SiC (ZrB_2–30SiC) was recently studied in the high-temperature, low-pressure dissociated air flow generated by the 1.2 MW Plasmatron facility of the von Kármán Institute for Fluid Dynamics (VKI). Plasmatron and arcjet facilities generate high-enthalpy, highly dissociated flows that better simulate the thermochemical environment expected in service on a hypersonic vehicle than do furnace environments. Results describing oxide surface properties, composition, and microstructure as a function of test time and Plasmatron conditions are presented in a separate publication [23]. Here we report emission spectroscopic measurements performed as an adjunct to this test series. These measurements were prompted by the observation of strong green fluorescence, suspected to originate from $BO_2(A^2\Pi_u \rightarrow X^2\Pi_g)$ emission, directly adjacent to UHTC specimen surfaces during exposure to the Plasmatron gas flow. Spectral emission data confirm this hypothesis and, additionally, capture emission from the $BO(A^2\Pi \rightarrow X^2\Sigma^+)$ system and the $B(^2S_{1/2} \rightarrow {}^2P^o_{1/2,3/2})$ transitions. Time-resolved emission measurements can follow the temporal evolution of emission intensities from these electronically excited boron species as the UHTC sample oxidizes. Because all boron species in the gas phase must originate from the volatilization of B_2O_3, such time-resolved spectra provide an in situ monitor for UHTC oxidation and independent data for correlation with oxide growth models.

II. Experiment

A. Test Specimens

UHTC specimens were hot pressed as thin disks, starting with commercial powders (H.C. Starck grade B ZrB_2 and grade UF-10 SiC) that were attrition milled using tungsten carbide media for two hours and dried by rotary evaporation. The dried powders were hot pressed in boron-nitride-coated graphite dies lined with graphite foil. The hot press was heated under vacuum (~20 Pa) at $\sim 20^\circ\text{C} \cdot \text{min}^{-1}$ to 1450°C, held for 1 h, then heated at the same rate to 1650°C and held for another hour. The hot press was then backfilled to 1 atm with argon and heated at $\sim 20^\circ\text{C} \cdot \text{min}^{-1}$ to a temperature of 1900°C, at which a pressure of 32 MPa was applied and the specimens held for 45 min. At the end of this hold time, the hot press was cooled at $\sim 20^\circ\text{C} \cdot \text{min}^{-1}$ to room temperature and, at ~1750°C, the load was removed. The pressed samples were approximately 3–4 mm thick with diameters of about 32 mm. The large faces of the hot-pressed disks were diamond ground flat and a 30 deg bevel was diamond ground into the disk edge so that the samples would fit into the standard ESA 50 mm stagnation point test fixture used in the Plasmatron facility.

Posttest samples were prepared for microscopy by cutting specimens perpendicular to their oxidized faces and polishing the cross sections to a 0.25 μm finish using diamond abrasives. Microstructure and composition characterization was performed using high-resolution field-emission scanning electron microscopy with a JEOL 6100 instrument (JEOL, Ltd., Tokyo, Japan) in conjunction with energy dispersive x-ray spectroscopy (EDAX, Mahwah, New Jersey).

B. Plasmatron Conditions

Plasma oxidation experiments were performed in air. The 1.2 MW Plasmatron facility at the von Kármán Institute [24,25] generates a high-enthalpy subsonic gas flow using inductive coupling. The plasma flow is directed through a quartz tube into a vacuum chamber in which test models and probes for measuring dynamic pressure and stagnation point heating rates are mounted on water-cooled arms that can be swung into and out of the flow. Test conditions are set by adjusting the generator power; the air mass flow rate, $\dot{m}$; the static pressure in the vacuum chamber, P_{stat}; and the exposure time in the flow. The cold-wall stagnation point heat flux, q_{cw}, and the dynamic pressure, P_{dyn}, are measured using water-cooled probes the same size and external shape as the test specimen holder so that important flow parameters (dynamic pressure, velocity gradient) are reproduced. Sample surface temperatures are measured with a two-color pyrometer (Marathon Series MR1SC, Raytek Corporation, Santa Cruz, California) at an acquisition rate of 1 Hz through a glass window at an incident angle 29 deg off-normal.

The data are presented for two UHTC specimens tested under nominally identical test conditions; see Table 1. The boundary-layer-edge enthalpy, gas temperature, and velocity are estimated to be approximately $25\ \text{kJ} \cdot \text{g}^{-1}$, 5800°C, and $130\ \text{m} \cdot \text{s}^{-1}$ based on computational fluid dynamics calculations performed at VKI (details of these computations are provided in a separate manuscript [23]). Under these conditions, molecular oxygen is completely dissociated and the number density of atomic oxygen and atomic nitrogen are approximately equal.

Sample 17 was used in preliminary calibration experiments associated with the earlier UHTC test series, during which it was exposed to air plasma flows under various test conditions (mass flow rates of 8 and $16\ \text{g} \cdot \text{s}^{-1}$, power levels varying between 150 and 200 kW, surface temperatures ranging from 1260 to 1400°C) for many (at least 10) minutes. As a result, the specimen surface was preoxidized, with a multilayer oxide structure as described in the Introduction. Sample 7 was a virgin specimen with no surface oxide layer present.

C. Emission Measurements

The emission from the hot gas in front of the test specimen was collected using the optical system shown in Fig. 1. The collection optics were aligned such that the optical axis was perpendicular to the plasma jet and parallel to the sample face along its symmetry plane, with the 0.4-mm-diam light collection volume tangent to the sample surface. The light emitted by the gas is collected by a spherical mirror, which images the emission, after a second reflection off a flat mirror and onto the entrance of an optical fiber. The fiber transmits the light to an Ocean Optics HR4000CG-UV-NIR spectrometer for the dispersion and recording of the emission spectrum.

This high-throughput spectrometer ($f/4$) images emission onto a 3648-element linear Si charge-coupled device (CCD) array over the 200–1100 nm wavelength range with a 300 groove/mm grating and a fixed 5 μm slit width, which provides a spectral resolution of 0.25 nm. The optical system was calibrated using a tungsten ribbon lamp (OSRAM ref. WI 17G). The spectral response of the system was determined for the wavelength interval of 350–800 nm, during which the calibration signal is sufficiently strong to be measured. Measured spectra were collected with a time resolution of 1 s.

III. Experimental Results

Pictures of the sample holder in the plasma flow were taken every second. Figure 2 compares two pictures taken 55 s after sample injection into the plasma stream; preoxidized sample 17 is on the left (Fig. 2a) and virgin sample 7 is on the right (Fig. 2b). The difference in the color of the gas surrounding the sample holder in the two images is obvious. A strong green fluorescence is seen clearly in Fig. 2b, but not in Fig. 2a. A similar green emission is well known in the field of boron combustion [26–29]. A small amount of green light was also observed at earlier times during the testing of sample 17, but it disappeared quickly. Sample 17 was tested before sample 7, and the same SiC cover was used for both experiments, indicating that the SiC cover does not produce this emission phenomenon

Table 1 Test conditions, where generator power = 220 kW, $P_{\text{stat}} = 10^4$ Pa, and $\dot{m} = 16\ \text{g} \cdot \text{s}^{-1}$ for all tests

Sample	q_{cw}, W cm^{-2}	P_{dyn}, Pa	T_w, °C	Time, min
17 (preoxidized)	120	39	1616	3:20
7 (virgin)	119	38	1602	5:10

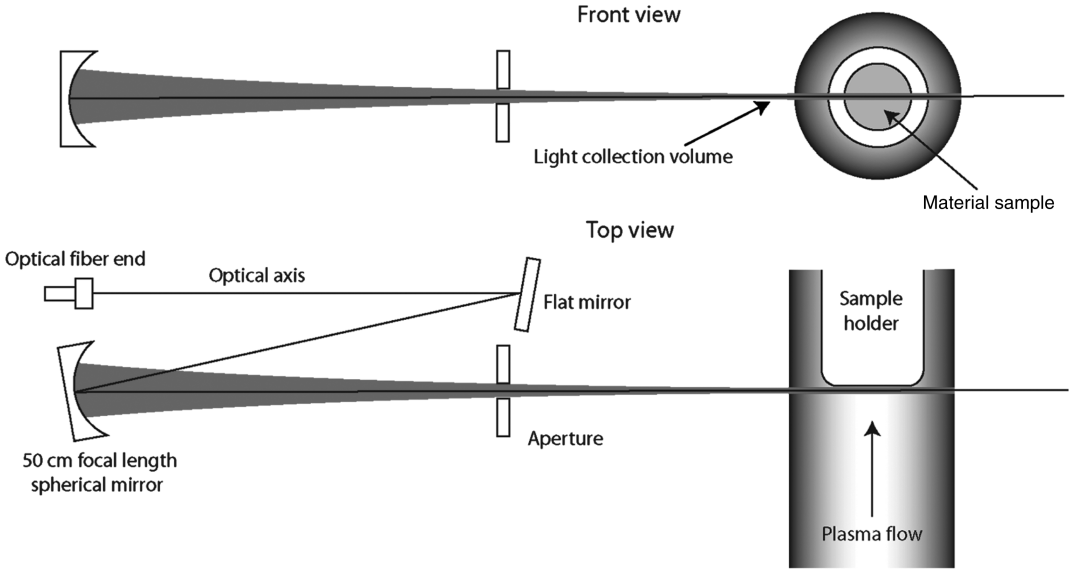

Fig. 1 Plasma emission collection system.

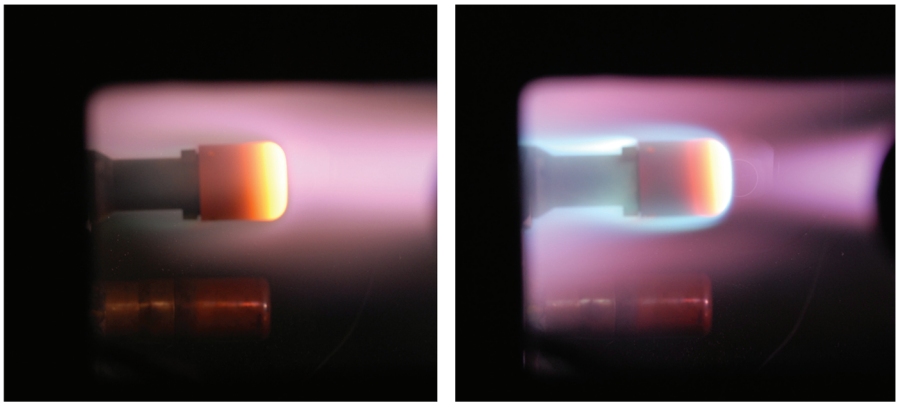

a) **b)**

Fig. 2 Samples during the Plasmatron testing 55 s after injection of the probe: a) sample 17, and b) sample 7.

Figures 3a and 3b show emission spectra collected 55 s after the injection of samples 17 and 7 into the plasma stream, corresponding in time to the photographs in Fig. 2. Figure 3a shows that emission originating from the doublet B ($^2S_{1/2} \rightarrow {}^2P^o_{1/2,3/2}$) transitions is present in the spectrum collected in front of sample 7 but not sample 17. The wavelength region below 350 nm is not calibrated, and the spectra in Fig. 3a are presented as raw signal in arbitrary units. In Fig. 3b, features associated with emission in the BO_2 ($A^2\Pi_u \rightarrow X^2\Pi_g$) and the BO ($A^2\Pi \rightarrow X^2\Sigma^+$) systems are evident in the spectrum collected in front of sample 7, but are absent in the spectrum collected in front of sample 17. Both spectra in Fig. 3b show strong emissions from the N_2^+ ($B^2\Sigma_u^+ \rightarrow X^2\Sigma_g^+$) first negative system in the 350–450 nm wavelength region. The N_2^+ first negative emission originates from the plasma freestream. Both spectra also show sharp emission lines near 589 and 546.7 nm. The former feature has a much larger intensity adjacent to the surface of sample 7 than sample 17 and is not present in the plasma freestream; it can be assigned to the strong Na ($^2P^o_{1/2,3/2} \rightarrow {}^2S_{1/2}$) doublet emission [30]. Further testing has shown that the apparent 546.7 nm emission feature results from a failed pixel in the linear CCD array.

Preliminary computations of the radiation emitted by the BO ($A^2\Pi \rightarrow X^2\Sigma^+$) system were performed. The emission of the two BO isotopes, ^{11}BO and ^{10}BO, was modeled independently using the spectroscopic constants of Mélen et al. [31]. Constants for states with vibrational quantum numbers υ' varying from 0 to 8 and υ'' from 0 to 8 for ^{11}BO and υ' from 0 to 8 and υ'' from 0 to 6 for ^{10}BO are available in this reference. These constants were extrapolated to vibrational quantum numbers up to 10 for the A state and up to 17 for the X state [32].

Figure 4 shows a comparison of a model BO ($A^2\Pi \rightarrow X^2\Sigma^+$) spectrum with the difference of the spectra measured in front of the two samples (i.e., the spectrum of sample 7 minus spectrum of sample 17) 55 s after injection into the plasma stream. Owing to the observation that the recorded spectra from the preoxidized and virgin samples agreed very well in regions above 750 nm in which boron species emission was absent, an unadjusted subtraction was made. This subtraction effectively removes the nitrogen emission features from the spectrum. The model spectrum was computed for a temperature of 6500 K using the hypotheses of local thermodynamic equilibrium emission and an optically thin medium. The two spectra were normalized individually by their peak values and offset for clarity.

Although the computed and measured spectral intensity distributions do not match well, the band structure is similar in the two spectra, particularly in the short wavelength region in which overlap with BO_2 features (whose bandheads are indicated in Fig. 4) is not important. The observed difference between the two intensity distributions could be caused by temperature and concentration nonuniformities in the flow, self-absorption along the line of sight, uncertainties in the spectroscopic constants used in the simulation, and/or the overlap of experimental BO features with other emission features, such as those of BO_2. Spectra computed for temperatures lower than 6500 K show worse agreement with the experimental intensity distribution in the short wavelength region, whereas

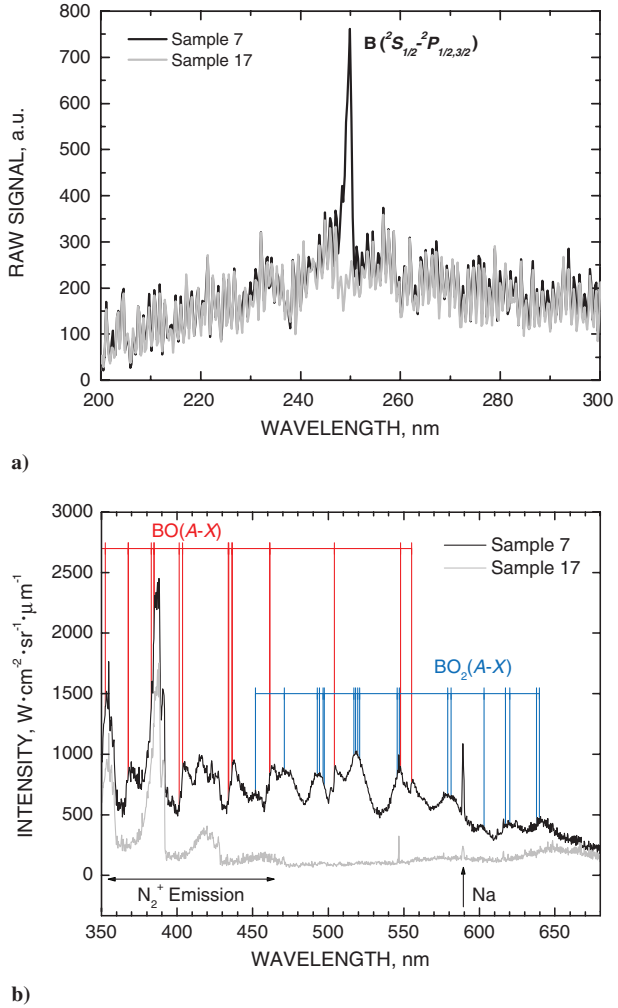

Fig. 3 Spectra collected 55 s after sample injection showing strong B, BO, and BO_2 emissions for sample 7 and the absence of boron emission signatures for sample 17: a) raw signal, and b) calibrated intensity. Boron oxide bandhead positions are from Spalding et al. [26].

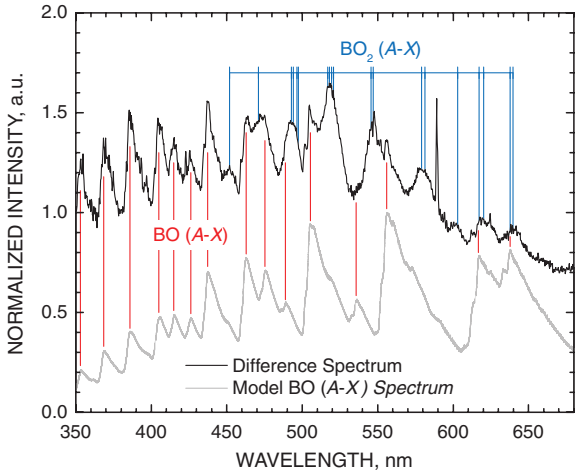

Fig. 4 Comparison of the computed (6500 K) BO ($A^2\Pi \rightarrow X^2\Sigma^+$) emission spectrum with the difference of the spectra measured in front of the two samples (i.e., the spectrum of sample 7 minus the spectrum of sample 17) 55 s after injection of the probe. The spectra are normalized independently by their peak values and are offset along the intensity axis for clarity. The red lines indicate the alignment of computed BO features with emission features in the experimental difference spectrum; the emission bandheads for the BO_2 ($A^2\Pi_u \rightarrow X^2\Pi_g$) system are from Spalding et al. [26].

spectra computed for higher temperatures show somewhat better agreement.

Based on computational fluid dynamics simulations performed at VKI, the plasma freestream temperature is estimated to be about ~6100 K [23]. However, the cylindrical emission collection volume is tangent to the ~1725 K sample surface (55 s into the test run) and the gas temperature in this part of the boundary layer is much lower, reaching only about 3000 K at a distance of 0.5 mm off the surface. The prominent short wavelength features in the experimental spectra suggests the possibility of a nonequilibrium "hot" vibrational distribution in the electronically excited BO. More data analysis and modeling are required before this possibility can be confirmed. Nevertheless, the comparison made in Fig. 4 underlines the strong contribution of BO emission to the observed fluorescence.

Figure 5 compares the transient surface temperatures measured on samples 7 and 17 with the temporal emission signatures of BO_2 (518.8 nm), BO (404.1 nm), and B (249.9 nm). These three wavelengths were chosen to minimize overlapping emission from multiple species. The pyrometer registers surface temperatures above 1100°C; the first portion of the temperature trace for sample 17 was lost during data acquisition. For sample 7, boron species emission signatures rise very rapidly as the surface temperature exceeds ~1250°C, about 40 s after sample injection into the stream. A quasi-steady surface temperature around 1600°C is attained about 80 s after sample injection, and all three boron species emission signatures decay steadily from this time onward. The calibrated BO_2 and BO emission intensities peak at intermediate times around 55 s. Although sample 17 experiences the same nominal heating condition resulting in similar surface temperatures, the boron emission features between 40 and 140 s are absent. After about 160 s, the emission levels in front of both samples become comparable. The test of sample 17 was ended early as no further evolution of the emission spectrum for the preoxidized sample was observed.

IV. Discussion

Thermodynamic data from [33] were used to calculate the pressures of gaseous species in equilibrium with liquid B_2O_3 at 1600°C to determine the species that are likely to volatilize from the specimen surface. Potential reactions among gaseous species were ignored for this analysis. The atmosphere was assumed to be monatomic oxygen at a pressure of 3×10^3 Pa ($P_O = 3 \times 10^3$ Pa or 0.02961 atm). Data for the standard Gibbs free energies of formation (ΔG_f^o) were extracted from the tables and used to calculate changes in the standard Gibbs free energy of reaction (ΔG_{rxn}^o), which were subsequently converted to pressures of the gaseous species.

The volatilization reaction $B_2O_{3(l)} + O_{(g)} \rightarrow 2BO_{2(g)}$ is considered as an example. At 1600°C, ΔG_{rxn}^o is 64.26 kJ · mol^{-1} and the equilibrium pressure of BO_2 (P_{BO_2}) was determined to be 2515 Pa from the relationship

$$\Delta G_{rxn}^o = -RT \ln\left(\frac{P_{BO_2}^2}{a_{B_2O_3} P_O}\right) \tag{2}$$

assuming unit activity for B_2O_3 ($a_{B_2O_3} = 1$). Similar calculations were performed for other boron species and the values are summarized in Table 2. Based on these calculations, the flux of boron species leaving the sample surface during the initial stages of oxidation in the Plasmatron should be predominantly BO_2 and B_2O_3, with much smaller contributions from BO and B_2O_2 and only trace amounts of B, B_2O, and B_2.

Emission spectroscopy detects the presence of electronically excited species. The $BO_2(A^2\Pi_u)$ [34], $BO(A^2\Pi)$ [35], and $B(^2S_{1/2})$ [30] excited states are located about 2.3, 3.0, and 5.0 eV above their respective ground states. It seems unlikely that any of these electronically excited boron species would volatilize from liquid B_2O_3 directly. The observed BO_2, BO, and B emissions must therefore result from some combination of gas-phase chemistry and energy transfer between boron volatiles in the ground state and freestream species. Based on the presence of large atomic oxygen and nitrogen concentrations at the sample surface, the observation of

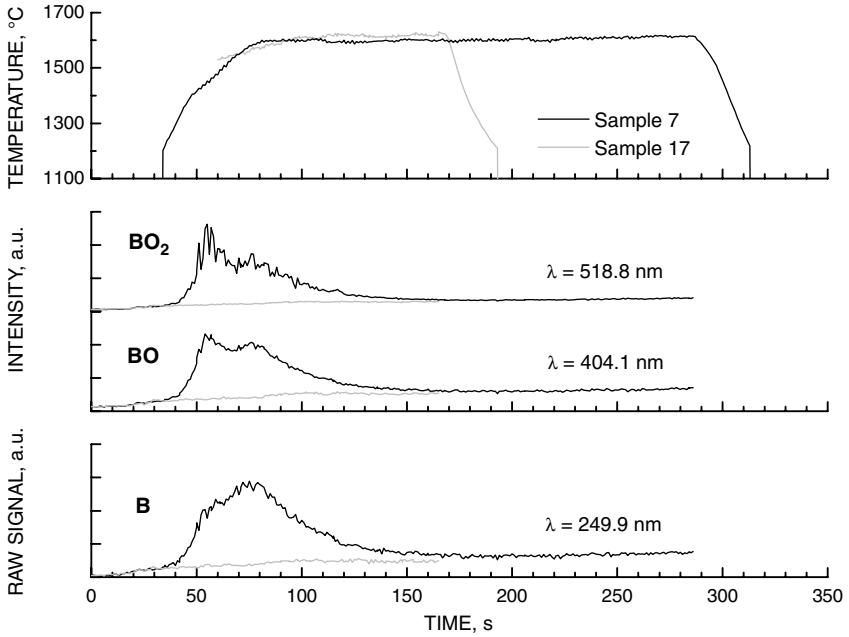

Fig. 5 Transient profiles of the surface temperature and the emission signatures of BO_2, BO, and B at 518.8, 404.1, and 249.9 nm, respectively.

boron atom emission at relatively low gas temperatures near the surface, and BO spectra that suggest nonthermal vibrational distributions, the boundary-layer gases immediately adjacent to the surface are probably not in thermochemical equilibrium. The observed electronically excited boron species emissions may therefore contain significant contributions from kinetically driven chemiluminescent reactions. The extent of thermal and chemical nonequilibrium in the emitting species cannot be evaluated without a coupled fluid dynamics and finite-rate chemistry computation of the plasma-generated species with the volatile boron species, a complicated problem beyond the scope of this paper.

The reaction of gas-phase B_2O_3 with atomic oxygen, $B_2O_3 + O \rightarrow 2BO_2$, is thermodynamically favored (negative ΔG^o_{rxn}) for all test temperatures [7]. The Gibbs free energy for the thermal dissociation of the larger boron oxide molecules becomes favorable with increasing temperature [7]: $B_2O \rightarrow BO + B$ at ~2915°C, $B_2O_2 \rightarrow 2BO$ at ~3030°C, $B_2O_3 \rightarrow BO + BO_2$ at ~3380°C, and $BO_2 \rightarrow BO + O$ at ~4015°C. Dissociation of these species is additionally promoted by collisions with highly energetic electronically and vibrationally excited nitrogen molecules produced by the Plasmatron. Atomic oxygen reactions with the smaller boron species are the most likely candidates for generating chemiluminscence. At 3000°C, the following reactions are both thermodynamically favored (negative Gibbs free energy) and sufficiently exothermic to produce the $BO_2(A^2\Pi_u)$ and $BO(A^2\Pi)$ states [7]: $B + O + M \rightarrow BO + M + 8.53$ eV, $B_2 + O \rightarrow BO + B + 5.45$ eV, $B_2O + O \rightarrow 2BO + 4.47$ eV, and $BO + O + M \rightarrow BO_2 + M + 5.79$ eV. (Here, M stands for the third body collision partner.)

The temporal evolutions of the boron species emission signatures shown in Fig. 5 are consistent with the general understanding of ZrB_2–SiC oxidation observed at different temperatures [11,17] and the reaction sequence for multilayer oxide formation at 1500°C described by Fahrenholtz [16]. The UHTC sample temperature rises very rapidly after injection into the plasma stream. Below about 800°C, both ZrB_2 and SiC oxidation is negligible. In the 800–1200°C temperature interval, the ZrB_2 oxidation rate increases whereas the SiC oxidation rate remains insignificant, leading to a surface oxide composed of ZrO_2 and SiC grains in a glassy B_2O_3 matrix. As the sample temperature rises through this regime, the B_2O_3 volatilization rate also accelerates, injecting significant amounts of boron oxide species into the boundary layer. As the temperature surpasses 1200°C, the oxidation rate of SiC becomes significant and the outer scale transforms into a borosilicate glass. Further increases in temperature raise the rates of both silicon oxide production and boron oxide loss, leading to the steady depletion of boron from the glassy scale. The volatilization rate of silicon oxide is many orders of magnitude lower than that of boron oxide in this temperature range. The resulting silica-rich outer oxide layer becomes an effective oxygen diffusion barrier and is responsible for the parabolic oxidation kinetics observed during steady-state oxidation experiments at temperatures near 1500°C [16]. As the silica-rich layer thickens, oxygen diffusion limitations lower the partial pressure of oxygen at the internal reaction interface, slowing production of B_2O_3. At sufficiently low oxygen partial pressures, the oxidation of ZrB_2 becomes insignificant relative to the (active) oxidation of SiC [16]. The flux of boron into the boundary layer decreases and eventually ceases, as boron is depleted from the outer glassy scale and is no longer replaced by B_2O_3 from in-depth ZrB_2 oxidation.

Table 2 Calculated pressures of volatile boron species in equilibrium with liquid B_2O_3 at 1600°C

Species	Pressure, Pa
BO_2	2215
B_2O_3	917
BO	1.1×10^{-3}
B_2O_2	3.6×10^{-7}
B	2.3×10^{-18}
B_2O	1.9×10^{-20}
B_2	1.3×10^{-38}

Figure 6 shows a cross-sectional FESEM micrograph of sample 7 after Plasmatron testing, together with corresponding EDS maps of elemental boron, zirconium, oxygen, and silicon. The EDS maps show the detection of each element as a white signal on a black background. Above the virgin material, the FESEM image reveals a ~30-μm-thick sublayer of oxidized material covered by a thin, uneven, glassy surface layer. In the virgin material, the EDS maps show the presence of boron, zirconium, and silicon and the relative absence of oxygen, as expected for unoxidized ZrB_2–30SiC material. The EDS maps show both zirconium and oxygen in the oxidized sublayer, indicating the oxidation of ZrB_2 to ZrO_2 and the presence of silicon and oxygen in the glassy outer layer corresponding to the formation of SiO_2 through the oxidation of SiC. The weakness of the EDS boron signal in both the oxidized sublayer and the outer glassy layer clearly indicate diminished boron

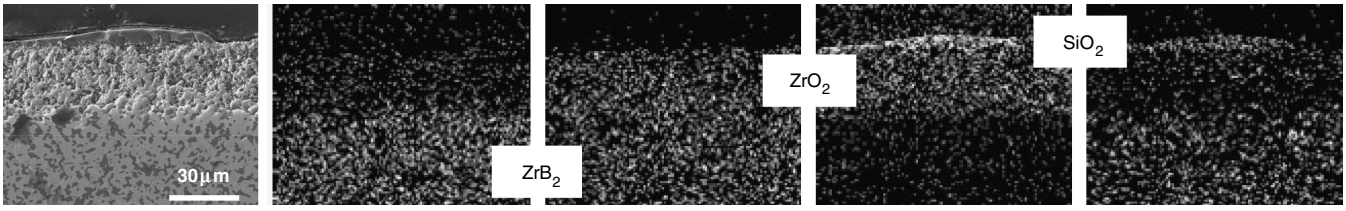

Fig. 6 FESEM micrograph and elemental EDS maps of the oxide layer formed on sample 7 after Plasmatron testing.

concentrations relative to the virgin material and correspond well with the scenario of boron oxide volatilization outlined earlier.

A surface temperature of ~1600°C is still moderate compared with the ambitious goal of sustained operation of UHTC components at 2000°C and higher [1,2]. As temperatures approach 2000°C, a similar volatilization of silicon species occurs and the outer silica-rich glassy layer recedes, leaving a porous zirconia (or hafnia in the case of HfB_2-based material) oxide scale [20,21,36]. It would be interesting to explore if similar spectroscopic emission diagnostics could be used to detect and track Si and SiO volatilization under such conditions.

V. Conclusions

The emission measurements presented here demonstrate that boron species can be detected in the gas phase at the surface of a ZrB_2–30SiC UHTC material exposed to an air plasma flow. Emissions originating from the BO_2 ($A^2\Pi_u \rightarrow X^2\Pi_g$) system, the BO ($A^2\Pi \rightarrow X^2\Sigma^+$) system, and the B ($^2S_{1/2} \rightarrow {}^2P^o_{1/2,3/2}$) doublet transitions were identified in spectra collected over the 200–800 nm wavelength range. Because all gas-phase boride species must ultimately originate from the sample, time-resolved emission spectra from electronically excited B, BO, and BO_2 molecules provide an in situ monitor for the oxidation of the ZrB_2–30SiC UHTC material. The rise and fall of these boron species emissions during the test series correlate well with theoretical models of the transient formation of complex oxide layers based on competing oxidation, diffusion, and vaporization processes. Posttest microscopy of the oxidized sample confirms the expected depletion of boron in the oxide scale sublayer beneath the outer silica-rich glass.

Because most UHTC materials (monolithic or coating) under development for leading-edge and control surface applications on hypersonic vehicles contain some boride constituents [1,2], emission spectroscopy is potentially broadly useful for following UHTC stability and performance in extreme oxidizing Plasmatron and arcjet test environments.

Acknowledgments

This research was supported by the Ceramics and Nonmetallic Materials Program of the U.S. Air Force Office of Scientific Research through contracts F49550-05-C-0020 (Marschall) and FA9550-06-0125 (Fahrenholtz and Hilmas), the National Science Foundation through grants DMR-0435856 (Marschall) and DMR-0346800 (Fahrenholtz and Zhu), and the European Office of Aerospace Research and Development through contract FA8655-06-1-3078 (Playez and Fletcher). The authors thank Dušan Pejaković of SRI for performing the FESEM and EDS measurements and Jan Thömel of VKI for computational estimates of the Plasmatron test conditions.

References

[1] Fuller, J., Blum, Y., and Marschall, J., "Topical Issue on Ultra-High-Temperature Ceramics," *Journal of the American Ceramic Society*, Vol. 91, No. 5, 2008, pp. 1397–1502. doi:10.1111/j.1551-2916.2008.02481.x

[2] Fuller, J., and Sacks, M., "Special Section: Ultra-High Temperature Ceramics," *Journal of Materials Science*, Vol. 39, No. 19, 2004, pp. 5885–6066. doi:10.1023/B:JMSC.0000041685.85043.34

[3] Fahrenholtz, W. G., Hilmas, G. E., Talmy, I. G., and Zaykoski, J. A., "Refractory Diborides of Zirconium and Hafnium," *Journal of the American Ceramic Society*, Vol. 90, No. 5, 2007, pp. 1347–1364. doi:10.1111/j.1551-2916.2007.01583.x

[4] Gasch, M., Johnson, S., and Marschall, J., "Thermal Conductivity Characterization of Hafnium Diboride-Based Ultra High Temperature Ceramics," *Journal of the American Ceramic Society*, Vol. 91, No. 5, 2008, pp. 1423–1432. doi:10.1111/j.1551-2916.2008.02364.x

[5] Zimmermann, J. W., Hilmas, G. E., and Fahrenholtz, W. G., "Thermophysical Properties of ZrB_2 and ZrB_2–SiC Ceramics," *Journal of the American Ceramic Society*, Vol. 91, No. 5, 2008, pp. 1405–1411. doi:10.1111/j.1551-2916.2008.02268.x

[6] Rizzo, H. F., "Oxidation of Boron at Temperatures Between 400 and 1300 °C in Air," *Boron-Synthesis, Structure, and Properties*, edited by J. A. Kohn, and W. F. Nye, Plenum, New York, 1968, pp. 175–189.

[7] Roine, A., HSC Chemistry for Windows, Ver. 5.11, Outokumpu Research Oy, Pori, Finland, 2006.

[8] Tripp, W. C., and Graham, H. C., "Thermogravimetric Study of the Oxidation of ZrB_2 in the Temperature Range of 800 to 1500 C," *Journal of the Electrochemical Society*, Vol. 118, No. 7, 1971, pp. 1195–1199. doi:10.1149/1.2408279

[9] Kuriakose, A. K., and Margrave, J. L., "The Oxidation Kinetics of Zirconium Diboride and Zirconium Carbide at High Temperatures," *Journal of the Electrochemical Society*, Vol. 111, No. 7, 1964, pp. 827–831. doi:10.1149/1.2426263

[10] Berkowitz-Mattuck, J. B., "High-Temperature Oxidation III. Zirconium and Hafnium Diborides," *Journal of the Electrochemical Society*, Vol. 113, 1966, pp. 908–914. doi:10.1149/1.2424154

[11] Monteverde, F., and Bellosi, A., "Oxidation of ZrB_2-Based Ceramics in Dry Air," *Journal of the Electrochemical Society*, Vol. 150, No. 11, 2003, pp. B552–B559. doi:10.1149/1.1618226

[12] Tripp, W. C., Davis, H. H., and Graham, H. C., "Effect of an SiC Addition on the Oxidation of ZrB_2," *Ceramic Bulletin*, Vol. 52, No. 8, 1973, pp. 612–616.

[13] Monteverde, F., and Savino, R., "Stability of Ultra-High Temperature ZrB_2–SiC Ceramics Under Simulated Atmospheric Re-Entry Conditions," *Journal of the European Ceramic Society*, Vol. 27, 2007, pp. 4797–4805. doi:10.1016/j.jeurceramsoc.2007.02.201

[14] Opeka, M. M., Talmy, I. G., Wuchina, E. J., Zaykoski, J. A., and Causey, S. J., "Mechanical, Thermal, and Oxidation Properties of Refractory Hafnium and Zirconium Compounds," *Journal of the European Ceramic Society*, Vol. 19, 1999, pp. 2405–2414. doi:10.1016/S0955-2219(99)00129-6

[15] Bull, J., "The Influence of SiC on the Ablation Response of Advanced Refractory Composite Materials," *19th Conference on Composite Materials and Structures*, Pt. 1, Advanced Materials Processes and Technology Information Analysis Center, Rome, NY, 1995, pp. 157–181.

[16] Fahrenholtz, W. G., "Thermodynamic Analysis of ZrB_2–SiC Oxidation: Formation of a SiC-Depleted Region," *Journal of the American Ceramic Society*, Vol. 90, No. 1, 2007, pp. 143–148. doi:10.1111/j.1551-2916.2006.01329.x

[17] Rezaie, A., Fahrenholtz, W. G., and Hilmas, G. E., "Evolution of Structure During the Oxidation of Zirconium Diboride-Silicon Carbide in Air up to 1500 °C," *Journal of the European Ceramic Society*, Vol. 27, 2007, pp. 2495–2501. doi:10.1016/j.jeurceramsoc.2006.10.012

[18] Monteverde, F., and Bellosi, A., "The Resistance to Oxidation of an HfB_2–SiC Composite," *Journal of the European Ceramic Society*, Vol. 25, May 2005, pp. 1025–1031.doi:10.1016/j.jeurceramsoc.2004.05.009

[19] Monteverde, F., and Scatteia, L., "Resistance to Thermal Shock and to Oxidation of Metal Diborides-SiC Ceramics for Aerospace Application," *Journal of the American Ceramic Society*, Vol. 90, No. 4, 2007, pp. 1130–1138. doi:10.1111/j.1551-2916.2007.01589.x

[20] Gasch, M., Ellerby, D., Irby, E., Beckman, S., Gusman, M., and Johnson, S., "Processing, Properties and Arc Jet Oxidation of Hafnium Diboride/Silicon Carbide Ultra High Temperature Ceramics," *Journal of Materials Science*, Vol. 39, No. 19, 2004, pp. 5925–5937. doi:10.1023/B:JMSC.0000041689.90456.af

[21] Opeka, M. M., Talmy, I. G., and Zaykoski, J. A., "Oxidation-Based Materials Selection for 2000°C+ Hypersonic Aerosurfaces: Theoretical Considerations and Historical Experience," *Journal of Materials Science*, Vol. 39, No. 19, 2004, pp. 5887–5904. doi:10.1023/B:JMSC.0000041686.21788.77

[22] Fahrenholtz, W. G., "The ZrB_2 Volatility Diagram," *Journal of the American Ceramic Society*, Vol. 88, No. 12, 2005, pp. 3509–3512. doi:10.1111/j.1551-2916.2005.00599.x

[23] Marschall, J., Pejaković, D. A., Fahrenholtz, W. G., Hilmas, G. E., Ridge, J., Fletcher, D. G., Asma, C. O., and Thömel, J., "Oxidation of ZrB_2–SiC Ultra-High Temperature Ceramic Composites in Dissociated Air," *Journal of Thermophysics and Heat Transfer* (to be published).

[24] Bottin, B., Carbonaro, M., Zemsch, S., and Degrez, G., "Aerothermodynamic Design of an Inductively Coupled Plasma Wind Tunnel," AIAA Paper 1997-2498, June 1997.

[25] Bottin, B., Paris, S., Van Der Haegen, V., and Carbonaro, M., "Experimental and Computational Determination of the VKI Plasmatron Operating Envelope," AIAA Paper 1999-3607, June 1999.

[26] Spalding, M. J., Krier, H., and Burton, R. L., "Boron Suboxides Measured During Ignition and Combustion of Boron in Shocked Ar/F/O_2 and Ar/N_2/O_2 Mixtures," *Combustion and Flame*, Vol. 120, 2000, pp. 200–210. doi:10.1016/S0010-2180(99)00082-6

[27] Yoshida, T., and Yuasa, S., "Effect of Water Vapor on Ignition and Combustion of Boron Lumps in an Oxygen Stream," *Proceedings of the Combustion Institute*, Vol. 28, 2000, pp. 2735–2741.

[28] Yuasa, S., and Isoda, H., "Ignition and Combustion of Small Boron Lumps in an Oxygen Stream," *Combustion and Flame*, Vol. 86, 1991, pp. 216–222. doi:10.1016/0010-2180(91)90101-G

[29] Yuasa, S., Yoshida, T., Kawashima, M., and Isoda, H., "Effects of Pressure and Oxygen Concentration on Ignition and Combustion of Boron in Oxygen/Nitrogen Mixture Streams," *Combustion and Flame*, Vol. 113, 1998, pp. 380–387. doi:10.1016/S0010-2180(97)00225-3

[30] Ralchenko, Y., Kramida, A. E., and Reader, J., NIST Atomic Spectra Database, Ver. 3.1.5, National Institute of Standards and Technology, Gaithersburg, MD, 2008.

[31] Mélen, F., Dubois, I., and Bredohl, H., "The *A*–*X* and *B*–*X* Transitions of BO," *Journal of Physics B: Atomic, Molecular and Optical Physics*, Vol. 18, 1985, pp. 2423–2432. doi:10.1088/0022-3700/18/12/019

[32] Coxon, J. A., Foster, S. C., and Naxakis, S., "Rotational Analysis of the $(A^2\Pi \rightarrow X^2\Sigma^+)$ Visible Band System of Boron Monoxide, BO," *Journal of Molecular Spectroscopy*, Vol. 105, No. 2, 1984, pp. 465–479. doi:10.1016/0022-2852(84)90234-0

[33] Chase, M. W., Jr., *NIST-JANAF Thermochemical Tables*, 4th ed., American Institute of Physics, New York, 1998.

[34] Johns, J. W. C., "The Absorption Spectrum of BO_2," *Canadian Journal of Physics*, Vol. 39, 1961, pp. 1738–1768.

[35] Herzberg, G., *Molecular Spectra and Molecular Structure I. Spectra of Diatomic Molecules*, 2nd ed., Krieger, Malabar, FL, 1989.

[36] Bronson, A., and Chessa, J., "An Evaluation of Vaporization Rates of SiO_2 and TiO_2 as Protective Coatings for Ultrahigh Temperature Ceramics," *Journal of the American Ceramic Society*, Vol. 91, No. 5, 2008, pp. 1448–1452. doi:10.1111/j.1551-2916.2008.02286.x